

# A Blind Multiscale Spatial Regularization Framework for Kernel-based Spectral Unmixing

Ricardo Augusto Borsoi, Tales Imbiriba, *Member, IEEE*, José Carlos Moreira Bermudez, *Senior Member, IEEE*,  
Cédric Richard, *Senior Member, IEEE*

**Abstract**—Introducing spatial prior information in hyperspectral imaging (HSI) analysis has led to an overall improvement of the performance of many HSI methods applied for denoising, classification, and unmixing. Extending such methodologies to nonlinear settings is not always straightforward, specially for unmixing problems where the consideration of spatial relationships between neighboring pixels might comprise intricate interactions between their fractional abundances and nonlinear contributions. In this paper, we consider a multiscale regularization strategy for nonlinear spectral unmixing with kernels. The proposed methodology splits the unmixing problem into two sub-problems at two different spatial scales: a coarse scale containing low-dimensional structures, and the original fine scale. The coarse spatial domain is defined using superpixels that result from a multiscale transformation. Spectral unmixing is then formulated as the solution of quadratically constrained optimization problems, which are solved efficiently by exploring a reformulation of their dual cost functions in the form of root-finding problems. Furthermore, we employ a theory-based statistical framework to devise a consistent strategy to estimate all required parameters, including both the regularization parameters of the algorithm and the number of superpixels of the transformation, resulting in a truly blind (from the parameters setting perspective) unmixing method. Experimental results attest the superior performance of the proposed method when comparing with other, state-of-the-art, related strategies.

**Index Terms**—Hyperspectral data, multiscale, spatial regularization, nonlinear unmixing, kernel methods.

## I. INTRODUCTION

Modern remote sensing greatly relies on hyperspectral (HS) image analysis to retrieve information about surface materials in many applications such as agriculture, surveillance and space exploration [1]. Specifically, reflectance measures can provide detailed information about the spectral signature of pure materials present on the surface of a target scene and their proportion for each pixel. Applications often, but not exclusively, associated with remote sensing trade poor spatial resolution for high spectral resolution due to physical limitations of imaging sensors and to the distance between the sensor and the target scene. Therefore, the measured reflectance of a given pixel is usually a mixture of the pure spectral signatures of materials existing in the corresponding area. *Spectral*

*unmixing* (SU) consists of extracting the pure component spectral signatures and their proportions (or abundances) for each pixel. The literature presents many mixing models to explain the observed reflectance as a mathematical function of the pure spectral components. The simplest form of such models is the *linear mixing model* (LMM) which confines the observed reflectance vectors into a convex hull whose extremities are the pure component spectral signatures, therefore, called endmembers. The LMM is effective in accurately modelling mixtures occurring in scenes where the materials of interest cover a large area with respect to the pixel size [2]. It however disregards more complex mixing phenomena such as non-linearity [2], [3] and spectral variability [4], [5], [6], [7], which often results in estimation errors being propagated throughout the unmixing process [8].

Nonlinear interactions between materials occur in many scenes where there is complex radiation scattering among several endmembers, such as in some vegetation areas [9]. In such situations, nonlinear mixing models must be considered [2], [10]. Several nonlinear SU strategies have been proposed in the literature, which can be roughly divided between model-based and model-free methods. Most model-based nonlinear SU algorithms assume that the mixing process that occurs in the scene is known a priori [11], [12], [13], [10], [2]. However, real mixing mechanisms can be very complex and prior knowledge about them is seldom available in practice. This led to the consideration of more flexible model-free nonlinear SU, which employ more flexible nonlinear mixing models that are able to represent generic functions. Prominent model-free strategies include the estimation of abundances as posterior class probabilities of a nonlinear classifier [14], the use of graph-based approximate geodesic distances [15], [16], and kernel-based algorithms [17], [18], [19], [20], [21]. Kernel-based methods provide non-parametric representations of functional spaces that are able to model arbitrary nonlinear mixtures [17], [18], [10], [2], [19], [20], [22]. This flexibility, allied to a good experimental performance has led to the wide application of kernel methods.

Despite the good results obtained with kernel-based unmixing methods [20], most algorithms fail to explore the high spatial regularity associated to many real world scenes. This property can be leveraged to improve the conditioning of the unmixing problem. Spatial regularization has already been shown to improve the performance of linear [23], [24] and sparse [25], [26] SU, as well as spectral-variability-aware SU [27], [28], [5], [29]. However, spatial information has seldom been enforced in nonlinear unmixing algorithms, partly

This work has been supported by the National Council for Scientific and Technological Development (CNPq).

R.A. Borsoi, T. Imbiriba and J.C.M. Bermudez are with the Department of Electrical Engineering, Federal University of Santa Catarina, Florianópolis, SC, Brazil. e-mail: raborsoi@gmail.com; talesim@gmail.com; j.bermudez@ieee.org.

C. Richard is with the Université Côte d'Azur, Nice, France (e-mail: cedric.richard@unice.fr), Lagrange Laboratory (CNRS, OCA).

Manuscript received Month day, year; revised Month day, year.

due to the challenges associated with more complex observation models. For instance, a spatial clustering approach was used in [30] to divide the image into different groups of pixels. SU was then performed using the P-linear mixing model in a Bayesian framework with a unique set of regularization parameters for each group. In [31] a *Total Variation* (TV) regularization was introduced in a regression-based kernel unmixing method [20], and a variable splitting approach was then used to solve the resulting optimization problem.

The TV regularization has been widely used in many HS imaging tasks since it promotes smooth image reconstructions while still allowing for sharp discontinuities [25]. However, TV regularization is not the most effective approach to extract spatial information from hyperspectral images. Regularization strategies exploiting nonlocal redundancy in images were recently considered for SU [32], leading to a better abundance estimation performance at the expense of a significant increase in computational complexity. In [33], a multiscale spatial regularization approach was proposed for sparse spectral unmixing. The multiscale approach led to improved results and smaller computational complexity when compared to TV regularization. The unmixing problem was split into two simpler problems in different image domains defined using a multiscale transformation. This transformation groups image pixels into contiguous regions using (over)-segmentation strategies such as the superpixel decomposition [33]. The multiscale regularization strategy was later extended in [34] to consider SU accounting for spectral variability. Despite the excellent results obtained with spatial regularization strategies, their performance usually depends on the careful selection of regularization parameters. This is specially important in multiscale strategies, which require a larger number of parameters. Determination of parameters for spatial regularization methods remains a challenging problem, and works applied to HSI are rare [26], [35].

In this paper, we propose a new multiscale spatial regularization approach for kernel-based nonlinear unmixing. Building upon the ideas proposed in [33], we employ a multiscale representation to divide the unmixing problem into two simpler problems in different scales. Though based on the same principle used in [33], devising kernel-based mixing models in multiple scales is more challenging than in the linear case. Moreover, we address the parameter adjustment problem differently from what has been done in previous multiscale SU formulations in [33], [34]. In this work we reformulate the SU problem at multiple scales by statistically characterizing not only the algorithm reconstruction error in both scales, but also the inter-scale interaction between the abundances and the nonlinear mixing contributions across the coarse and fine image domains. This formulation leads to physically motivated constraints which are leveraged to devise the *Blind Multiscale Unmixing Algorithm for Nonlinear Mixtures* (BMUA-N), in which all the parameters are determined automatically from the observed data. Thus, the proposed strategy benefits from an improved quality without the need for *ad hoc* parameter adjustment such as in TV-based works.

We formulate the resulting unmixing problem as a sequence of two optimization problems with quadratic equality con-

straints. These non-convex problems are solved by reformulating the dual problems in the form of low-dimensional root finding problems, which can be solved in very few iterations using a multidimensional bisection algorithm.

Simulations with synthetic and real datasets illustrate the effectiveness of the proposed methodology in producing piecewise smooth solutions while preserving sharp discontinuities existing in the image. This leads to more accurate unmixing results when compared to TV-based strategies, with less computational complexity and without the need for *ad hoc* parameter adjustment.

This manuscript is organized as follows. In Section II we discuss the main concepts related to regression-based kernel unmixing. In Section III we present the proposed kernel-based multiscale unmixing strategy. The automatic parameter setting methodology is presented in Section IV and the solution for the proposed optimization problems is discussed in Section V. In Section VI we propose a method for designing the multiscale transformation to yield spectral homogeneity. Experimental results are presented and discussed in Section VII. They are followed by concluding remarks in Section VIII.

## II. KERNEL-BASED UNMIXING

### A. Kernel-based mixture model

In this section we review the standard kernel-based mixture model introduced in [20] and discuss the main theoretical aspects of kernel machines. As in [20], we assume that each  $L$ -band observed pixel  $\mathbf{y}_n \in \mathbb{R}^L$  in an HSI can be modeled as a function of the endmember spectra as follows:

$$y_{n,\ell} = \psi_{\mathbf{a}_n}(\tilde{\mathbf{m}}_\ell) + e_{n,\ell}, \quad \ell = 1, \dots, L \quad (1)$$

where  $y_{n,\ell}$  is the  $\ell$ -th entry of vector  $\mathbf{y}_n$ ,  $\tilde{\mathbf{m}}_\ell \in \mathbb{R}^{1 \times P}$  is the  $\ell$ -th row of the endmember matrix  $\mathbf{M} \in \mathbb{R}^{L \times P}$  with  $P$  spectral signatures of pure materials in the scene. Function  $\psi_{\mathbf{a}_n}$  is an unknown nonlinear function defining the interactions between endmember spectra parameterized by their fractional abundances  $\mathbf{a}_n \in \mathbb{R}^P$ .  $e_{n,\ell}$  includes the observation noise and modeling errors. The problem that arises is to find a functional  $\psi_{\mathbf{a}_n}$  that can accurately represent the different and complex types of light-endmember interactions often occurring in real scenes. Since the type of nonlinearity is rarely known in practice, a popular solution is to search for kernel-based smooth function representations whose parameters can be learned directly from the data [2], [3].

In [20], [31] the authors considered a semi-parametric kernel-based model consisting of a linear trend parameterized by the abundance vector plus an additive nonlinear fluctuation. The model, which allows the quantification of the abundance vectors during the unmixing process, is given by

$$\psi_{\mathbf{a}_n}(\tilde{\mathbf{m}}_\ell) = \tilde{\mathbf{m}}_\ell \mathbf{a}_n + \psi_n(\tilde{\mathbf{m}}_\ell) \quad (2)$$

with  $\psi_n : \mathbb{R}^P \rightarrow \mathbb{R}$  an arbitrary smooth function belonging to a Reproducing Kernel Hilbert Space (RKHS) denoted by  $\mathcal{H}$  and defined over a nonempty compact set  $\mathcal{M} \subset \mathbb{R}^P$ . This assumption allows for the kernel machinery (i.e., via the kernel trick) to obtain accurate solutions to the unmixing problem.

The theory of positive definite kernels emerged from the study of positive definite integral operators [36], and was further generalized in the study of positive definite matrices [37]. It has been established that, to every positive definite function  $\kappa(\cdot, \cdot) : \mathcal{M} \times \mathcal{M} \rightarrow \mathbb{R}$ , defined over a non-empty compact set  $\mathcal{M} \subset \mathbb{R}^P$ , there corresponds one and only one class of real-valued functions on  $\mathcal{M}$  forming a Hilbert space  $\mathcal{H}$  endowed with a uniquely defined inner product  $\langle \cdot, \cdot \rangle_{\mathcal{H}}$ , and admitting  $\kappa$  as a *reproducing kernel* (r.k.) [38]. Space  $\mathcal{H}$  is called a RKHS if its evaluation functional  $\delta_{\widetilde{\mathbf{m}}}$  is a linear and continuous (or equivalently bounded) functional for every  $\widetilde{\mathbf{m}} \in \mathcal{M}$ , thus, admitting  $\kappa$  as its unique kernel. As a consequence of the Riesz representation theorem [39, p. 188],  $\kappa(\cdot, \widetilde{\mathbf{m}})$  is the representer of evaluation of any functional  $\psi \in \mathcal{H}$ , such that the *reproducing property*

$$\psi(\widetilde{\mathbf{m}}) = \langle \psi, \kappa(\cdot, \widetilde{\mathbf{m}}) \rangle_{\mathcal{H}} \quad (3)$$

holds, for all  $\psi \in \mathcal{H}$  and all  $\widetilde{\mathbf{m}} \in \mathcal{M}$ . Furthermore, since  $\kappa(\cdot, \widetilde{\mathbf{m}}) \in \mathcal{H}$  for all  $\widetilde{\mathbf{m}}, \widetilde{\mathbf{m}}' \in \mathcal{M}$  we also have

$$\kappa(\widetilde{\mathbf{m}}, \widetilde{\mathbf{m}}') = \langle \kappa(\cdot, \widetilde{\mathbf{m}}), \kappa(\cdot, \widetilde{\mathbf{m}}') \rangle_{\mathcal{H}}. \quad (4)$$

The RKHS  $\mathcal{H}$  is then formed by a class of functions generated by all functions of the form  $\psi(\cdot) = \sum_j \alpha_j \kappa(\cdot, \widetilde{\mathbf{m}}_j)$ , with norm defined by  $\|\psi\|_{\mathcal{H}}^2 = \sum_i \sum_j \alpha_i \alpha_j \kappa(\widetilde{\mathbf{m}}_i, \widetilde{\mathbf{m}}_j)$ .

In the context of machine learning, kernel methods are often related with the concept of building a high dimensional feature space  $\mathcal{H}$ , and a mapping

$$\begin{aligned} \Phi : \mathcal{M} &\longrightarrow \mathcal{H} \\ \widetilde{\mathbf{m}} &\longmapsto \Phi(\widetilde{\mathbf{m}}) \end{aligned} \quad (5)$$

with inner product defined as  $\kappa(\widetilde{\mathbf{m}}, \widetilde{\mathbf{m}}') = \langle \Phi(\widetilde{\mathbf{m}}), \Phi(\widetilde{\mathbf{m}}') \rangle_{\mathcal{H}}$ . If  $\kappa$  is a r.k. of  $\mathcal{H}$ , then  $\mathcal{H}$  is a RKHS and also a feature space of  $\kappa$  with  $\Phi(\widetilde{\mathbf{m}}) = \kappa(\cdot, \widetilde{\mathbf{m}})$ . In this case  $\Phi$  is called the *canonical feature map* [40, p. 120]. This leads to the so-called “*kernel trick*” allowing one to compute inner products of data mapped into higher, or even infinite, dimensional feature spaces by evaluating a real function  $\kappa(\widetilde{\mathbf{m}}_i, \widetilde{\mathbf{m}}_j)$  in the input space.

Although the literature proposes a variety of kernel functions elaborated during the past two decades of intense research activity [41], [42], [43], in this work we restrain ourselves to the polynomial kernel due to its intimate relation with multiple scattering phenomena known to exist in the interaction between light and the materials in the scene. Thus, the polynomial kernel is given by

$$\kappa(\widetilde{\mathbf{m}}_i, \widetilde{\mathbf{m}}_j) = (\widetilde{\mathbf{m}}_i^\top \widetilde{\mathbf{m}}_j + c)^d \quad (6)$$

where  $d$  is the polynomial degree and  $c \geq 0$  is a real number. Due to relevant findings reported in [44] concerning the order of multiple reflection models and the good results obtained in [31], in this paper we assume  $d = 2$  and  $c = 1$  in all simulations.

### B. LS-SVR-based unmixing

In [20] the authors proposed to solve the unmixing problem accounting for the model in (1)–(2) by considering a multi-kernel generalization of standard least-squares support vector

regression (LS-SVR) methods [45]. The resulting optimization problem is given by

$$\begin{aligned} (\hat{\mathbf{a}}_n, \hat{\psi}_n) = \arg \min_{\mathbf{a}_n, \psi_n} & \frac{1}{2} \left( \|\mathbf{a}_n\|^2 + \|\psi_n\|_{\mathcal{H}}^2 + \frac{1}{\mu} \|\boldsymbol{\xi}_n\|_2^2 \right) \\ \text{subject to} & \quad \mathbf{a}_n \geq \mathbf{0}, \mathbf{1}^\top \mathbf{a}_n = 1, \text{ and} \\ & \quad \xi_{n,\ell} = y_{n,\ell} - \mathbf{a}_n^\top \widetilde{\mathbf{m}}_\ell - \psi(\widetilde{\mathbf{m}}_\ell). \end{aligned} \quad (7)$$

where  $\hat{\mathbf{a}}_n$  and  $\hat{\psi}_n$  are the estimated abundance vector and nonlinear function for the  $n$ -th pixel.

Problem (7) is solved using standard dual formulation based on the Lagrangian [20]. Although problem (7) presents an effective way of modeling both the linear trend and the nonlinear mixing occurring in a given pixel, it fails to impose any smooth structure over the abundance estimation within neighboring pixels.

Standard regularization approaches such as the TV have considered an additional term to the cost function in problem (7) that penalizes spatial discontinuities in the abundance maps [31]. However, as discussed in the introduction, this strategy is not the most effective in exploring spatial information contained in the image. Besides, it introduces an additional parameter that must be carefully tuned in order to achieve good performance.

In the following, we present a multiscale formulation for the nonlinear mixing model in (1)–(2) that enables us to better exploit the spatial regularity in HSIs, leading to improved results when compared to the TV-based strategy. Compared to linear unmixing, the application of a multiscale formulation to kernel-based nonlinear unmixing leads to specific challenges that need to be addressed. This is specially true in the present work, as quadratic equality constraints need to be reformulated to allow for the automatic determination of the parameters, and thus for a blind algorithm as detailed in Section IV.

## III. A MULTISCALE NONLINEAR MIXING MODEL

The incorporation of spatial information in the design of nonlinear SU algorithms through traditional spatial regularization (e.g. Tikhonov or Total Variation) leads to large scale optimization problems, and is not entirely efficient in capturing spatial contextual information in HSIs. Furthermore, determining the regularization parameters is very difficult in practice. Motivated by the results in [33], [34], we propose to introduce spatial information into the SU problem by dividing it into two consecutive steps. First, we represent the nonlinear mixing process in an approximation (coarse) spatial scale ( $\mathcal{C}$ ) which preserves relevant inter-pixel spatial contextual information. Pixels in the coarse spatial scale can be then unmixed independently from each other. The recovered coarse abundance maps are then mapped back to the original image domain ( $\mathcal{D}$ ) and used as prior information to regularize the second unmixing process applied to the original image to promote spatial dependency between neighboring pixels.

### A. Unmixing in the coarse scale

Denote the HSI and the abundance map for all pixels by  $\mathbf{Y} = [\mathbf{y}_1, \dots, \mathbf{y}_N]$  and  $\mathbf{A} = [\mathbf{a}_1, \dots, \mathbf{a}_N]$ , respectively.

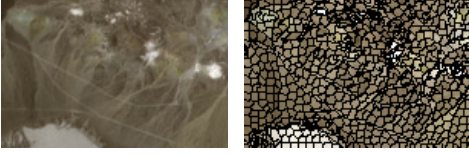


Figure 1. Cuprite image (left) and its superpixel decomposition (right).

We consider a dimensionality reduction transformation  $\mathbf{W} \in \mathbb{R}^{N \times K}$ ,  $K < N$ , constructed based on relevant contextual inter-pixel information present in the observed image  $\mathbf{Y}$ , that maps both the HSI and the abundance map to the approximation domain. The transformed matrices are given by

$$\mathbf{Y}_C = \mathbf{Y}\mathbf{W}; \quad \mathbf{A}_C = \mathbf{A}\mathbf{W}, \quad (8)$$

where  $\mathbf{Y}_C = [\mathbf{y}_{C_1}, \dots, \mathbf{y}_{C_K}] \in \mathbb{R}^{L \times K}$  and  $\mathbf{A}_C = [\mathbf{a}_{C_1}, \dots, \mathbf{a}_{C_K}] \in \mathbb{R}^{P \times K}$  are, respectively, the HSI and the abundance matrix in the coarse approximation scale.

Various methods can be used to construct the transformation  $\mathbf{W}$ . Specifically,  $\mathbf{W}$  must group pixels that are spatially adjacent and spectrally similar and must respect image borders by not grouping pixels corresponding to different image structures or features. Following the same approach as in [33], [34], we consider the superpixel decomposition of the image  $\mathbf{Y}$  for the transformation  $\mathbf{W}$ . Besides satisfying the criteria outlined above, multiscale decompositions based on superpixel algorithms have shown excellent performance in SU considering both sparsity [33] and variability of the endmembers [34]. Superpixel algorithms group image pixels into different spatially compact neighborhoods with similar spectral information [46], decomposing the image into a set of contiguous homogeneous regions whose size and regularity are controlled by adjusting a set of parameters. Furthermore, the superpixel decomposition can be computed very efficiently by employing low-cost algorithms such as the SLIC [46]. The transformation  $\mathbf{W}$  is thus constructed such that  $\mathbf{Y}\mathbf{W}$  computes the superpixel decomposition of the image  $\mathbf{Y}$  and returns the average of all pixels inside each superpixel.

The transformation  $\mathbf{W}$  is thus constructed such that  $\mathbf{Y}\mathbf{W}$  computes the superpixel decomposition of the image  $\mathbf{Y}$ , and returns the average of all pixel vectors inside each superpixel as the superpixel vector. The superpixel decomposition of the Cuprite hyperspectral image is illustrated in Figure 1.

Considering the nonlinear observation model (1), the transformed image in (8) leads to an equivalent mixing model in the coarse spatial domain, which is given by:

$$\begin{aligned} y_{C_i, \ell} &= \frac{1}{|\mathcal{N}_i|} \sum_{n \in \mathcal{N}_i} (\tilde{\mathbf{m}}_\ell \mathbf{a}_n + \psi_n(\tilde{\mathbf{m}}_\ell) + e_{n, \ell}) \\ &= \tilde{\mathbf{m}}_\ell \mathbf{a}_{C_i} + \psi_{C_i}(\tilde{\mathbf{m}}_\ell) + \frac{1}{|\mathcal{N}_i|} \sum_{n \in \mathcal{N}_i} e_{n, \ell} \end{aligned} \quad (9)$$

where  $y_{C_i, \ell}$  is the  $\ell$ -th entry of  $\mathbf{y}_{C_i}$ ,  $\mathcal{N}_i$  is the set of indexes of the pixels contained within the  $i$ -th superpixel,  $|\cdot|$  denotes the cardinality of a set, and  $\mathbf{a}_{C_i}$  and  $\psi_{C_i}$ , given by

$$\mathbf{a}_{C_i} = \frac{1}{|\mathcal{N}_i|} \sum_{n \in \mathcal{N}_i} \mathbf{a}_n, \quad \psi_{C_i}(\tilde{\mathbf{m}}_\ell) = \frac{1}{|\mathcal{N}_i|} \sum_{n \in \mathcal{N}_i} \psi_n(\tilde{\mathbf{m}}_\ell)$$

for  $i = 1, \dots, K$ , denote the fractional abundances and nonlinear contributions at the coarse spatial scale.

Following the observation model (9), the unmixing problem at the coarse spatial scale can be formulated following a similar approach to the LS-SVR-based SU formulation presented in Section II-B, given by the following optimization problem:

$$\begin{aligned} \{\hat{\mathbf{a}}_{C_i}, \hat{\psi}_{C_i}\} &= \arg \min_{\{\mathbf{a}_{C_i}, \psi_{C_i}\}} \frac{1}{2} \sum_{i=1}^K (\|\psi_{C_i}\|_{\mathcal{H}}^2 + \|\mathbf{a}_{C_i}\|_2^2) \quad (10) \\ \text{subject to } &\mathbf{a}_{C_i} \geq \mathbf{0}, \mathbf{1}^\top \mathbf{a}_{C_i} = 1, \quad i = 1, \dots, K \\ &\boldsymbol{\xi}_{C_i} = \mathbf{y}_{C_i} - \mathbf{M} \mathbf{a}_{C_i} - \psi_{C_i}(\mathbf{M}), \quad i = 1, \dots, K \\ &\frac{1}{K} \sum_{i=1}^K \|\boldsymbol{\xi}_{C_i}\|_2^2 = C_0 \end{aligned}$$

where  $\hat{\mathbf{a}}_{C_i}$  and  $\hat{\psi}_{C_i}$  are the estimated abundance vector and nonlinear function for the  $i$ -th superpixel and  $\psi_{C_i}(\mathbf{M}) = [\psi_{C_i}(\tilde{\mathbf{m}}_1), \dots, \psi_{C_i}(\tilde{\mathbf{m}}_L)]^\top$ . Parameter  $C_0$  is a positive constant that constrains the reconstruction error of the algorithm, and operates in an analogous manner to a regularization parameter. Differently from (7), we opted in (10) to limit the reconstruction error using an equality constraint instead of directly adding  $\|\boldsymbol{\xi}_{C_i}\|_2^2$ ,  $i = 1, \dots, K$  as a regularizer in the cost function. The rationale is that, unlike the regularization parameter  $\mu$  in (7), the constant  $C_0$  has a clear physical interpretation. This characteristic is exploited in the next section where we present a proper methodology for automatically setting  $C_0$ .

### B. Unmixing in the image domain

The abundance maps estimated at the coarse spatial scale, denoted by  $\mathbf{A}_C = [\mathbf{a}_{C_1}, \dots, \mathbf{a}_{C_K}]$ , can next be used to regularize the original unmixing problem. To this end, we convert the abundance map from the coarse approximation domain  $\mathcal{C}$  back to the original image domain  $\mathcal{D}$  as:

$$\hat{\mathbf{A}}_{\mathcal{D}} = \hat{\mathbf{A}}_{\mathcal{C}} \mathbf{W}^*. \quad (11)$$

Matrix  $\mathbf{W}^* \in \mathbb{R}^{K \times N}$  is a conjugate transformation to  $\mathbf{W}$ , and takes the image from the coarse domain  $\mathcal{C}$  back to the original (uniform) image domain. This is performed by attributing the value  $\hat{\mathbf{a}}_{C_i}$  to all pixels in  $\hat{\mathbf{A}}_{\mathcal{D}}$  that lie within the  $i$ -th superpixel. Thus,  $\hat{\mathbf{A}}_{\mathcal{D}}$  can be viewed as a coarse version of  $\hat{\mathbf{A}}$  in the original image domain.

After computing  $\hat{\mathbf{A}}_{\mathcal{D}}$  using (11), the SU problem for all pixels in the original image domain is given by:

$$\begin{aligned} \{\hat{\mathbf{a}}_n, \hat{\psi}_n\} &= \arg \min_{\{\mathbf{a}_n, \psi_n\}} \frac{1}{2} \sum_{n=1}^N \|\psi_n\|_{\mathcal{H}}^2 \quad (12) \\ \text{subject to } &\mathbf{a}_n \geq \mathbf{0}, \mathbf{1}^\top \mathbf{a}_n = 1, \quad n = 1, \dots, N \\ &\boldsymbol{\xi}_n = \mathbf{y}_n - \mathbf{M} \mathbf{a}_n - \psi_n(\mathbf{M}), \quad n = 1, \dots, N \\ &\frac{1}{N} \sum_{n=1}^N \|\boldsymbol{\xi}_n\|_2^2 = C_1, \quad \frac{1}{N} \sum_{n=1}^N \|\mathbf{a}_n - \hat{\mathbf{a}}_{\mathcal{D}_n}\|_2^2 = C_2 \end{aligned}$$

where  $\hat{\mathbf{a}}_n$  and  $\hat{\psi}_n$  are the estimated abundance vector and nonlinear function for the  $n$ -th pixel in the original image domain,  $\psi_n(\mathbf{M}) = [\psi_n(\tilde{\mathbf{m}}_1), \dots, \psi_n(\tilde{\mathbf{m}}_L)]^\top$ , and  $C_1, C_2$  are

positive constants that constrain the reconstruction error and the abundance variability across scales. Again, as in (10), we use equality constraints instead of regularization terms in the cost function due to the easier interpretation of  $C_1$  and  $C_2$  when compared to regularization parameters. This improved interpretability is exploited in the next section to provide a methodology for automatically adjusting these constants. We note that the nonlinear equality constraints make the optimization problems (10) and (12) non-convex. An efficient algorithm will be proposed in Section V to address this issue.

#### IV. DETERMINING THE REGULARIZATION CONSTANTS

A significant challenge in regularized unmixing algorithms consists in determining the regularization constants. The proposed formulation requires the selection of  $C_0$ ,  $C_1$  and  $C_2$  in problems (10) and (12). Most works assume that the regularization constants can be determined empirically and a priori. However, given their great impact on the performance of the algorithms, it is desirable to have theoretically sound means for selecting these parameters.

Constant  $C_0$  in (10) reflects the average noise power in the coarse image scale. Constants  $C_1$  and  $C_2$  in (12) reflect, respectively, the average noise power in the detail scale and the average energy of the differences between the fractional abundances and their estimates in the coarse domain.

We define these constants as statistical means as follows:

$$\begin{aligned} C_0 &= \mathbb{E} \left\{ \frac{1}{K} \sum_{i=1}^K \|\mathbf{y}_{C_i} - \mathbf{M} \mathbf{a}_{C_i} - \psi_{C_i}(\mathbf{M})\|_2^2 \right\} \\ &= \mathbb{E} \left\{ \frac{1}{K} \sum_{i=1}^K \|e_{C_i}\|_2^2 \right\} \end{aligned} \quad (13)$$

$$\begin{aligned} C_1 &= \mathbb{E} \left\{ \frac{1}{N} \sum_{n=1}^N \|\mathbf{y}_n - \mathbf{M} \mathbf{a}_n - \psi_n(\mathbf{M})\|_2^2 \right\} \\ &= \mathbb{E} \left\{ \frac{1}{N} \sum_{n=1}^N \|e_n\|_2^2 \right\} \end{aligned} \quad (14)$$

$$C_2 = \mathbb{E} \left\{ \frac{1}{N} \sum_{n=1}^N \|\mathbf{a}_n - \mathbf{a}_{\mathcal{D}_n}\|_2^2 \right\} \quad (15)$$

where  $\mathbb{E}\{\cdot\}$  is the expected value operator with respect to the true distribution of the parameters within the brackets, and  $e_n$  and  $e_{C_i}$  are the errors related to the fine and coarse domains of the  $n$ -th pixel and  $i$ -th superpixel respectively. In this case, the quadratic constraints in problems (10) and (12) can be seen as approximations to the above expected values.

Constants  $C_0$  and  $C_1$  depend directly on the noise level and modeling errors represented by  $e_n$ . We write

$$\mathbf{e}_n = \mathbf{e}_{0,n} + \mathbf{e}_{\psi,n} \quad (16)$$

where  $\mathbf{e}_{0,n}$  is a Gaussian noise term with zero mean and covariance  $\Sigma_e$ , and  $\mathbf{e}_{\psi,n}$  represents modeling errors. Before proceeding, we make the following assumptions:

- A1) The additive noise is spatially uncorrelated, i.e.  $\mathbb{E}\{\mathbf{e}_{0,n}^\top \mathbf{e}_{0,m}\} = 0, \forall n \neq m$ .
- A2) The noise and modeling errors  $\mathbf{e}_{0,n}$  and  $\mathbf{e}_{\psi,n}$  are uncorrelated.
- A3) The modeling errors  $\mathbf{e}_{\psi,n}$  are assumed to be spatially correlated and approximately constant within each superpixel, that is:

$$\mathbf{e}_{\psi,n} \approx \mathbf{e}_{\psi,m}, \quad \forall m, n \in \mathcal{N}_i, \quad i = 1, \dots, K. \quad (17)$$

This hypothesis is motivated from the fact that the nonlinear contributions in the mixing model are themselves spatially smooth [47], [48], which reflects in the modeling errors.

- A4) The expected value of the modeling error's norm is the same for all pixels, and is represented as

$$\mathbb{E} \{ \|\mathbf{e}_{\psi,n}\|_2^2 \} = \sigma_{e,\psi}^2, \quad n = 1, \dots, N. \quad (18)$$

- A5) The noise covariance matrix is the same for all image pixels, i.e.

$$\begin{aligned} \mathbb{E} \{ \mathbf{e}_{0,i} \mathbf{e}_{0,i}^\top \} &= \mathbb{E} \{ \mathbf{e}_{0,j} \mathbf{e}_{0,j}^\top \}, \quad 1 \leq i, j \leq N \\ &= \Sigma_e. \end{aligned} \quad (19)$$

We denote the average size of each superpixel by  $S = N/K$ .

In the following, we will evaluate the expectations in (13)–(15) in order to provide well-founded means to evaluate the constants  $C_0$ ,  $C_1$  and  $C_2$ .

##### A. Determining the constant $C_1$

Using hypothesis A1, A2 and A4, constant  $C_1$  can be computed as:

$$\begin{aligned} C_1 &= \mathbb{E} \left\{ \frac{1}{N} \sum_{n=1}^N \|\mathbf{e}_{0,n} + \mathbf{e}_{\psi,n}\|_2^2 \right\} \\ &\stackrel{(A2)}{=} \frac{1}{N} \sum_{n=1}^N \left( \mathbb{E} \{ \|\mathbf{e}_{0,n}\|_2^2 \} + \mathbb{E} \{ \|\mathbf{e}_{\psi,n}\|_2^2 \} \right) \\ &= \text{tr}\{\Sigma_e\} + \sigma_{e,\psi}^2. \end{aligned} \quad (20)$$

##### B. Determining the constant $C_0$

Constant  $C_0$  can be derived in a similar way by assuming A1–A4:

$$\begin{aligned} C_0 &= \mathbb{E} \left\{ \frac{1}{K} \sum_{i=1}^K \|e_{C_i}\|_2^2 \right\} \\ &= \mathbb{E} \left\{ \frac{1}{K} \sum_{i=1}^K \left\| \frac{1}{|\mathcal{N}_i|} \sum_{n \in \mathcal{N}_i} (\mathbf{e}_{0,n} + \mathbf{e}_{\psi,n}) \right\|_2^2 \right\} \\ &= \mathbb{E} \left\{ \frac{1}{K} \sum_{i=1}^K \frac{1}{|\mathcal{N}_i|^2} \left( \left\| \sum_{n \in \mathcal{N}_i} \mathbf{e}_{0,n} \right\|_2^2 + \left\| \sum_{n \in \mathcal{N}_i} \mathbf{e}_{\psi,n} \right\|_2^2 \right. \right. \\ &\quad \left. \left. + 2 \sum_{n \in \mathcal{N}_i} \sum_{m \in \mathcal{N}_i} \langle \mathbf{e}_{0,n}, \mathbf{e}_{\psi,m} \rangle \right) \right\} \\ &\stackrel{(A2)}{=} \frac{1}{K} \sum_{i=1}^K \frac{1}{|\mathcal{N}_i|^2} \sum_{n \in \mathcal{N}_i} \mathbb{E} \{ \|\mathbf{e}_{0,n}\|_2^2 \} \end{aligned}$$

$$+ \frac{1}{K} \sum_{i=1}^K \frac{1}{|\mathcal{N}_i|^2} \mathbb{E} \left\{ \left\| \sum_{n \in \mathcal{N}_i} \mathbf{e}_{\psi,n} \right\|_2^2 \right\} \quad (21)$$

The modeling errors are not uncorrelated and zero mean in each superpixel. By approximating  $K^{-1} \sum_{i=1}^K |\mathcal{N}_i|^{-1} \simeq S^{-1}$  and using hypothesis A3 and equation (17),  $C_0$  can be approximated as

$$\begin{aligned} C_0 &\simeq \frac{1}{S} \text{tr}\{\mathbf{\Sigma}_e\} + \frac{1}{K} \sum_{i=1}^K \frac{1}{|\mathcal{N}_i|^2} \sum_{n \in \mathcal{N}_i} \mathbb{E} \left\{ |\mathcal{N}_i| \|\mathbf{e}_{\psi,n}\|_2^2 \right\} \\ &\simeq \frac{1}{S} \text{tr}\{\mathbf{\Sigma}_e\} + \sigma_{e,\psi}^2. \end{aligned} \quad (22)$$

Note that this shows that the modeling errors are more significant relative to the noise at the coarse spatial scale. This is because the contribution of the noise is reduced by a factor of  $S$  whereas the modeling errors retain the same energy.

### C. Determining the constant $C_2$

The constant  $C_2$  is slightly more challenging to compute than the previous ones. We denote the left pseudo-inverse of  $\mathbf{M}$  as  $\mathbf{M}^\dagger \in \mathbb{R}^{P \times L}$ , that is,  $\mathbf{M}^\dagger \mathbf{M} = \mathbf{I}_P$ ). Then, we can consider the following quantity:

$$\begin{aligned} &\mathbb{E} \left\{ \frac{1}{N} \sum_{n=1}^N \|\mathbf{M}^\dagger (\mathbf{y}_n - \mathbf{y}_{\mathcal{D}_n})\|^2 \right\} \\ &= \mathbb{E} \left\{ \frac{1}{N} \sum_{n=1}^N \left\| \mathbf{M}^\dagger (\mathbf{M} \mathbf{a}_n + \mathbf{e}_n + \psi_n(\mathbf{M}) \right. \right. \\ &\quad \left. \left. - \mathbf{M} \mathbf{a}_{\mathcal{D}_n} - \psi_{C_n}^*(\mathbf{M}) - \frac{1}{|\mathcal{N}_n|} \sum_{i \in \mathcal{N}_n} \mathbf{e}_i \right\|^2 \right\} \end{aligned} \quad (23)$$

In order to proceed, we make one additional assumption:

A5) We consider the vectors  $\mathbf{a}_n - \mathbf{a}_{\mathcal{D}_n}$ ,  $\mathbf{M}^\dagger (\psi_n(\mathbf{M}) - \psi_{C_n}(\mathbf{M}))$  and  $\mathbf{M}^\dagger (\mathbf{e}_n - \frac{1}{|\mathcal{N}_n|} \sum_{i \in \mathcal{N}_n} \mathbf{e}_i)$  to be mutually uncorrelated and zero-mean.

This hypothesis is reasonable since each of those terms comprises fluctuations between the coarse and fine spatial scales, which can be expected to be zero mean. Thus, by noting that

$$\mathbb{E} \left\{ \|\mathbf{M}^\dagger (\mathbf{M} \mathbf{a}_n - \mathbf{M} \mathbf{a}_{\mathcal{D}_n})\|^2 \right\} = \mathbb{E} \left\{ \|\mathbf{a}_n - \mathbf{a}_{\mathcal{D}_n}\|^2 \right\}. \quad (24)$$

and using A5 we can write (23) as

$$\begin{aligned} &\mathbb{E} \left\{ \frac{1}{N} \sum_{n=1}^N \|\mathbf{M}^\dagger (\mathbf{y}_n - \mathbf{y}_{\mathcal{D}_n})\|^2 \right\} = \mathbb{E} \left\{ \frac{1}{N} \sum_{n=1}^N \|\mathbf{a}_n - \mathbf{a}_{\mathcal{D}_n}\|^2 \right\} \\ &\quad + \mathbb{E} \left\{ \frac{1}{N} \sum_{n=1}^N \|\mathbf{M}^\dagger (\psi_n(\mathbf{M}) - \psi_{C_n}(\mathbf{M}))\|^2 \right\} \\ &\quad + \mathbb{E} \left\{ \frac{1}{N} \sum_{n=1}^N \left\| \mathbf{M}^\dagger \left( \mathbf{e}_n - \frac{1}{|\mathcal{N}_n|} \sum_{i \in \mathcal{N}_n} \mathbf{e}_i \right) \right\|^2 \right\}. \end{aligned} \quad (25)$$

In the following, we will expand the last term on the right hand side of (25). Using A1–A4, the summand for each pixel can be written as

$$\mathbb{E} \left\| \mathbf{M}^\dagger \left( \mathbf{e}_n - \frac{1}{|\mathcal{N}_n|} \sum_{i \in \mathcal{N}_n} \mathbf{e}_i \right) \right\|^2$$

$$\begin{aligned} &= \mathbb{E} \left\| \mathbf{M}^\dagger \left( \mathbf{e}_{0,n} + \mathbf{e}_{\psi,n} - \frac{1}{|\mathcal{N}_n|} \sum_{i \in \mathcal{N}_n} (\mathbf{e}_{0,i} + \mathbf{e}_{\psi,i}) \right) \right\|^2 \\ &\stackrel{(A2)}{=} \mathbb{E} \left\| \mathbf{M}^\dagger \left( \mathbf{e}_{0,n} - \frac{1}{|\mathcal{N}_n|} \sum_{i \in \mathcal{N}_n} \mathbf{e}_{0,i} \right) \right\|^2 \\ &\quad + \mathbb{E} \left\| \mathbf{M}^\dagger \left( \mathbf{e}_{\psi,n} - \frac{1}{|\mathcal{N}_n|} \sum_{i \in \mathcal{N}_n} \mathbf{e}_{\psi,i} \right) \right\|^2 \end{aligned} \quad (26)$$

Using hypothesis A3 and equation (17), the second term of (26) can be approximated as

$$\mathbb{E} \left\| \mathbf{M}^\dagger \left( \mathbf{e}_{\psi,n} - \frac{1}{|\mathcal{N}_n|} \sum_{i \in \mathcal{N}_n} \mathbf{e}_{\psi,i} \right) \right\|^2 \approx 0 \quad (27)$$

This can be intuitively reasoned by accounting for the spatial correlation of the modeling errors, where  $\mathbf{e}_{\psi,n}$  in each pixel is very similar to the average of the modeling errors in its respective superpixel. This leads to

$$\begin{aligned} &\mathbb{E} \left\| \mathbf{M}^\dagger \left( \mathbf{e}_n - \frac{1}{|\mathcal{N}_n|} \sum_{i \in \mathcal{N}_n} \mathbf{e}_i \right) \right\|^2 \\ &\simeq \mathbb{E} \left\| \mathbf{M}^\dagger \left( \mathbf{e}_{0,n} - \frac{1}{|\mathcal{N}_n|} \sum_{i \in \mathcal{N}_n} \mathbf{e}_{0,i} \right) \right\|^2 \\ &= \mathbb{E} \left\| \mathbf{M}^\dagger \mathbf{e}_{0,n} \left( 1 - \frac{1}{|\mathcal{N}_n|} \right) - \mathbf{M}^\dagger \frac{1}{|\mathcal{N}_n|} \sum_{i \in \mathcal{N}_n \setminus \{n\}} \mathbf{e}_{0,i} \right\|^2 \\ &\stackrel{(A1)}{=} \mathbb{E} \left\| \mathbf{M}^\dagger \mathbf{e}_{0,n} \left( 1 - \frac{1}{|\mathcal{N}_n|} \right) \right\|^2 + \mathbb{E} \left\| \mathbf{M}^\dagger \frac{1}{|\mathcal{N}_n|} \sum_{i \in \mathcal{N}_n \setminus \{n\}} \mathbf{e}_{0,i} \right\|^2 \\ &\stackrel{(A1)}{=} \mathbb{E} \left\| \mathbf{M}^\dagger \mathbf{e}_{0,n} \left( 1 - \frac{1}{|\mathcal{N}_n|} \right) \right\|^2 + \frac{1}{|\mathcal{N}_n|^2} \sum_{i \in \mathcal{N}_n \setminus \{n\}} \mathbb{E} \|\mathbf{M}^\dagger \mathbf{e}_{0,i}\|^2 \\ &\stackrel{(A5)}{=} \mathbb{E} \|\mathbf{M}^\dagger \mathbf{e}_{0,n}\|^2 \left( 1 - \frac{1}{|\mathcal{N}_n|} \right)^2 + \frac{|\mathcal{N}_n| - 1}{|\mathcal{N}_n|^2} \mathbb{E} \|\mathbf{M}^\dagger \mathbf{e}_{0,n}\|^2 \\ &= \mathbb{E} \|\mathbf{M}^\dagger \mathbf{e}_{0,n}\|^2 \frac{|\mathcal{N}_n| - 1}{|\mathcal{N}_n|} \end{aligned} \quad (28)$$

where " $\setminus$ " denotes the set difference operator.

Since the noise statistics are spatially invariant, see A5,

$$\begin{aligned} \mathbb{E} \|\mathbf{M}^\dagger \mathbf{e}_{0,n}\|^2 &= \mathbb{E} \left\{ \text{tr} \{ \mathbf{M}^\dagger \mathbf{e}_n \mathbf{e}_n^\top (\mathbf{M}^\dagger)^\top \} \right\} \\ &= \|\mathbf{M}^\dagger \mathbf{\Sigma}_e^{1/2}\|_F^2 \end{aligned} \quad (29)$$

and, by approximating the superpixel sizes by their average value (i.e.  $|\mathcal{N}_n| \simeq S$ ), we can approximate (26) as

$$\begin{aligned} &\mathbb{E} \left\{ \frac{1}{N} \sum_{n=1}^N \left\| \mathbf{M}^\dagger \left( \mathbf{e}_n - \frac{1}{|\mathcal{N}_n|} \sum_{i \in \mathcal{N}_n} \mathbf{e}_i \right) \right\|^2 \right\} \\ &\simeq \|\mathbf{M}^\dagger \mathbf{\Sigma}_e^{1/2}\|_F^2 \frac{S-1}{S}. \end{aligned} \quad (30)$$

Finally, approximating the expectations with respect to  $\mathbf{a}_n$  and  $\psi_n$  by their instantaneous values and using the estimates  $\hat{\mathbf{a}}_{\mathcal{D}_n}$  and  $\hat{\psi}_{C_n}$  obtained as solutions to the optimization problem (10), equation (25) can be approximated as

$$\begin{aligned} &\frac{1}{N} \sum_{n=1}^N \|\mathbf{a}_n - \hat{\mathbf{a}}_{\mathcal{D}_n}\|^2 \simeq \frac{1}{N} \sum_{n=1}^N \|\mathbf{M}^\dagger (\mathbf{y}_n - \mathbf{y}_{\mathcal{D}_n})\|^2 \\ &\quad - \frac{1}{N} \sum_{n=1}^N \|\mathbf{M}^\dagger (\psi_n(\mathbf{M}) - \hat{\psi}_{C_n}(\mathbf{M}))\|^2 \end{aligned}$$

$$- \|M^\dagger \Sigma_e^{1/2}\|_F^2 \frac{S-1}{S}. \quad (31)$$

#### D. The updated fine scale optimization problem

Using these results, we can substitute the second quadratic equality constraint of problem (12) by (31), resulting in the following problem

$$\begin{aligned} \arg \min_{\{\mathbf{a}_n, \psi_n\}} & \frac{1}{2} \sum_{n=1}^N \|\psi_n\|_{\mathcal{H}}^2 \\ \text{subject to } & \mathbf{a}_n \geq 0, \mathbf{1}^\top \mathbf{a}_n = 1, \quad n = 1, \dots, N \\ & \boldsymbol{\xi}_n = \mathbf{y}_n - \mathbf{M} \mathbf{a}_n - \psi_n(\mathbf{M}), \quad n = 1, \dots, N \\ & \frac{1}{N} \sum_{n=1}^N \|\boldsymbol{\xi}_n\|_2^2 = C_1 \\ & \frac{1}{N} \sum_{n=1}^N \|\mathbf{a}_n - \hat{\mathbf{a}}_{\mathcal{D}_n}\|_2^2 = C_Y - C_E \\ & - \frac{1}{N} \sum_{n=1}^N \|M^\dagger(\psi_n(\mathbf{M}) - \hat{\psi}_{\mathcal{C}_n}(\mathbf{M}))\|^2 \end{aligned} \quad (32)$$

where constants  $C_Y$  and  $C_E$  are defined as

$$\begin{aligned} C_Y &= \frac{1}{N} \sum_{n=1}^N \|M^\dagger(\mathbf{y}_n - \mathbf{y}_{\mathcal{D}_n})\|^2, \\ C_E &= \|M^\dagger \Sigma_e^{1/2}\|_F^2 \frac{S-1}{S}. \end{aligned} \quad (33)$$

Defining

$$\boldsymbol{\xi}_{\psi,n} = M^\dagger(\psi_n(\mathbf{M}) - \hat{\psi}_{\mathcal{C}_n}(\mathbf{M})), \quad n = 1, \dots, N \quad (34)$$

and multiplying the quadratic constraints by  $N/2$ , we can represent problem (32) equivalently as

$$\begin{aligned} \arg \min_{\{\mathbf{a}_n, \psi_n\}} & \frac{1}{2} \sum_{n=1}^N \|\psi_n\|_{\mathcal{H}}^2 \\ \text{subject to } & \mathbf{a}_n \geq 0, \mathbf{1}^\top \mathbf{a}_n = 1, \quad n = 1, \dots, N \\ & \boldsymbol{\xi}_n = \mathbf{y}_n - \mathbf{M} \mathbf{a}_n - \psi_n(\mathbf{M}), \quad n = 1, \dots, N \\ & \frac{1}{2} \sum_{n=1}^N \|\boldsymbol{\xi}_n\|_2^2 = \frac{N}{2} C_1 \\ & \frac{1}{2} \sum_{n=1}^N (\|\mathbf{a}_n - \hat{\mathbf{a}}_{\mathcal{D}_n}\|_2^2 + \|\boldsymbol{\xi}_{\psi,n}\|^2) = \frac{N}{2} (C_Y - C_E) \\ & \boldsymbol{\xi}_{\psi,n} = M^\dagger(\psi_n(\mathbf{M}) - \hat{\psi}_{\mathcal{C}_n}(\mathbf{M})), \quad n = 1, \dots, N \end{aligned} \quad (35)$$

Problem (35) can now be used instead of (12) to perform unmixing in the original spatial scale.

## V. SOLVING THE OPTIMIZATION PROBLEMS

The quadratic equality constraints in problems (10) and (35) make the optimization problems non-convex. Furthermore, the functional form of the variables  $\psi_{\mathcal{C}_i}$  and  $\psi_n$  makes them hard to tackle in their primal form. Thus, we resort to a Lagrangian relaxation and solve the dual problem, which results in a convex and finite-dimensional optimization problem [49], [42].

#### A. The coarse scale dual problem

The Lagrangian of (10) is given by

$$\begin{aligned} \mathcal{J}_{\mathcal{C}} = \sum_{i=1}^K & \left\{ \frac{1}{2} \|\psi_{\mathcal{C}_i}\|_{\mathcal{H}}^2 + \|\mathbf{a}_{\mathcal{C}_i}\|_2^2 + \frac{\mu_0}{2} (\|\boldsymbol{\xi}_{\mathcal{C}_i}\|_2^2 - C_0) \right. \\ & + \lambda_{\mathcal{C}_i} (\mathbf{1}^\top \mathbf{a}_{\mathcal{C}_i} - 1) - \gamma_{\mathcal{C}_i}^\top \mathbf{a}_{\mathcal{C}_i} \\ & \left. - \beta_{\mathcal{C}_i}^\top (\boldsymbol{\xi}_{\mathcal{C}_i} - \mathbf{y}_{\mathcal{C}_i} + \mathbf{M} \mathbf{a}_{\mathcal{C}_i} + \psi_{\mathcal{C}_i}(\mathbf{M})) \right\} \end{aligned} \quad (36)$$

where  $\mu_0, \beta_{\mathcal{C}_i}, \lambda_{\mathcal{C}_i}$  and  $\gamma_{\mathcal{C}_i} \geq \mathbf{0}$  are the Lagrange multipliers.

The optimality conditions with respect to the primal variables are given by:

$$\begin{aligned} \mathbf{a}_{\mathcal{C}_i}^* &= \mathbf{M}^\top \beta_{\mathcal{C}_i}^* + \gamma_{\mathcal{C}_i}^* - \lambda_{\mathcal{C}_i}^* \mathbf{1} \\ \psi_{\mathcal{C}_i}^* &= \sum_{\ell=1}^L \beta_{\mathcal{C}_i, \ell}^* \kappa(\cdot, \tilde{\mathbf{m}}_\ell) \\ \boldsymbol{\xi}_{\mathcal{C}_i}^* &= \frac{1}{\mu_0} \beta_{\mathcal{C}_i}^*. \end{aligned} \quad (37)$$

By replacing these solutions into the Lagrangian in (36), we can derive the dual optimization problem, which is given by

$$\begin{aligned} \max_{\mu_0} \max_{\boldsymbol{\omega}_{\mathcal{C}}} & \sum_{i=1}^K \left( \boldsymbol{\omega}_{\mathcal{C}_i}^\top \mathbf{B}_{\mathcal{C}}(\mu_0) \boldsymbol{\omega}_{\mathcal{C}_i} + \mathbf{c}_{\mathcal{C}_i}^\top \boldsymbol{\omega}_{\mathcal{C}_i} \right) - \frac{\mu_0}{2} K C_0 \\ \text{subject to } & \gamma_{\mathcal{C}_i} \geq \mathbf{0}, \quad i = 1, \dots, K \end{aligned} \quad (38)$$

where  $\boldsymbol{\omega}_{\mathcal{C}} = [\boldsymbol{\omega}_1^\top, \dots, \boldsymbol{\omega}_K^\top]^\top$ ,  $\boldsymbol{\omega}_{\mathcal{C}_i} = [\beta_{\mathcal{C}_i}^\top, \gamma_{\mathcal{C}_i}^\top, \lambda_{\mathcal{C}_i}]^\top$  is the vector of dual variables, and  $\mathbf{B}_{\mathcal{C}}$  and  $\mathbf{c}_{\mathcal{C}_i}$  are given by

$$\mathbf{B}_{\mathcal{C}}(\mu_0) = -\frac{1}{2} \begin{bmatrix} \mathbf{K} + \frac{1}{\mu_0} \mathbf{I} + \mathbf{M} \mathbf{M}^\top & \mathbf{M} & -\mathbf{M} \mathbf{1} \\ \mathbf{M}^\top & \mathbf{I} & -\mathbf{1} \\ -\mathbf{1}^\top \mathbf{M}^\top & -\mathbf{1}^\top & P \end{bmatrix} \quad (39)$$

$$\mathbf{c}_{\mathcal{C}_i} = [\mathbf{y}_{\mathcal{C}_i}^\top \mid \mathbf{0} \mid -1]^\top. \quad (40)$$

#### B. The fine scale dual problem

The Lagrangian of (35) is given by

$$\begin{aligned} \mathcal{J}_{\mathcal{D}} = \sum_{n=1}^N & \left\{ \frac{1}{2} \|\psi_n\|_{\mathcal{H}}^2 + \frac{\mu_1}{2} (\|\boldsymbol{\xi}_n\|_2^2 - C_1) + \lambda_n (\mathbf{1}^\top \mathbf{a}_n - 1) \right. \\ & + \frac{\mu_2}{2} (\|\mathbf{a}_n - \hat{\mathbf{a}}_{\mathcal{D}_n}\|_2^2 - C_Y + \|\boldsymbol{\xi}_{\psi,n}\|^2 + C_E) \\ & + \boldsymbol{\mu}_{3,n}^\top (M^\dagger(\psi_n(\mathbf{M}) - \hat{\psi}_{\mathcal{C}_n}(\mathbf{M})) - \boldsymbol{\xi}_{\psi,n}) \\ & \left. - \beta_n^\top (\boldsymbol{\xi}_n - \mathbf{y}_n + \mathbf{M} \mathbf{a}_n + \psi_n(\mathbf{M})) - \gamma_n^\top \mathbf{a}_n \right\} \end{aligned} \quad (41)$$

where  $\mu_1, \mu_2, \boldsymbol{\mu}_{3,n}, \beta_n, \gamma_n$  and  $\lambda_n$  are the Lagrange multipliers.

We can derive optimality conditions with respect to the primal variables:

$$\begin{aligned} a_n^* &= \hat{a}_{\mathcal{D}_n} + \frac{1}{\mu_2} \left( \mathbf{M}^\top \beta_n^* + \gamma_n^* - \lambda_n^* \mathbf{1} \right) \\ \psi_n^* &= \sum_{\ell=1}^L \beta_{n,\ell}^* \kappa(\cdot, \tilde{\mathbf{m}}_\ell) - \sum_{\ell=1}^L [[\mu_{3,n}^*]^\top \mathbf{M}^\dagger]_\ell \kappa(\cdot, \tilde{\mathbf{m}}_\ell) \\ \xi_n^* &= \frac{1}{\mu_1^*} \beta_n^* \\ \xi_{\psi,n}^* &= \frac{1}{\mu_2^*} \mu_{3,n}^* \end{aligned} \quad (42)$$

where  $[\cdot]_\ell$  denotes the  $\ell$ -th position of a vector.

Substituting the solution to the primal problem in the Lagrangian, the dual problem is given by

$$\begin{aligned} \max_{\mu_1, \mu_2} \max_{\boldsymbol{\omega}} \sum_{n=1}^N \left( \boldsymbol{\omega}_n^\top \mathbf{B}(\mu_1, \mu_2) \boldsymbol{\omega}_n + \mathbf{c}_n^\top \boldsymbol{\omega}_n \right) \\ - \frac{N}{2} (\mu_1 C_1 + \mu_2 C_Y - \mu_2 C_E) \end{aligned} \quad (43)$$

subject to  $\gamma_n \geq 0, n = 1, \dots, N$

where  $\boldsymbol{\omega} = [\boldsymbol{\omega}_1^\top, \dots, \boldsymbol{\omega}_N^\top]^\top$  is a vector containing the dual variables, with entries given by  $\boldsymbol{\omega}_n = [\beta_n^\top, \mu_{3,n}^\top, \gamma_n^\top, \lambda_n^\top]^\top$ . The terms  $\mathbf{B}(\mu_1, \mu_2)$  and  $\mathbf{c}_n$  are defined in (44).

Since problems (38) and (43) are Lagrangian dual problems, they are concave with respect to all variables [49]. However, they are nonlinear and thus computationally intensive to solve given their dimensionality. Note that, although these problems are nonlinear and thus cannot be solved directly, the cost function of (43) (resp. (38)) becomes quadratic when  $\mu_1$  and  $\mu_2$  (resp.  $\mu_0$ ) are fixed. This will allow us to propose an efficient algorithm to solve these problems.

### C. An efficient solution to the Lagrangian dual problem

In order to devise an efficient algorithm for solving problems (38) and (43), we first note that the purpose of the maximization with respect to  $\mu_0, \mu_1$  and  $\mu_2$  is to ensure that the quadratic equality constraints in the primal problems (10) and (35) are satisfied. Thus, we will attempt to write the dual problem in an equivalent form that will make this explicit and allow for a simpler solution.

The optimality conditions for the coarse scale dual problem (38) with respect to  $\mu_0$  are obtained by differentiating the cost function and setting it equal to zero, which gives

$$g_0(\mu_0; \boldsymbol{\omega}) = 0 \quad (45)$$

where function  $g_0$  is defined as

$$g_0(\mu_0; \boldsymbol{\omega}) = \frac{1}{\mu_0^2} \sum_{i=1}^K \|\beta_{\mathcal{C}_i}\|_2^2 - K C_0. \quad (46)$$

Similarly, for the fine scale dual problem (43) the optimality conditions with respect to  $\mu_1$  and  $\mu_2$  can be obtained by differentiating the cost function and setting it equal to zero, which gives

$$\begin{cases} g_1(\mu_1, \mu_2; \boldsymbol{\omega}) = 0 \\ g_2(\mu_1, \mu_2; \boldsymbol{\omega}) = 0 \end{cases} \quad (47)$$

where functions  $g_1$  and  $g_2$  are defined as

$$\begin{aligned} g_1(\mu_1, \mu_2; \boldsymbol{\omega}) &= \frac{1}{\mu_1^2} \sum_{n=1}^N \|\beta_n\|_2^2 - N C_1 \\ g_2(\mu_1, \mu_2; \boldsymbol{\omega}) &= \frac{1}{\mu_2^2} \sum_{n=1}^N \left( \|\mathbf{M}^\top \beta_n + \gamma_n - \lambda_n \mathbf{1}\|_2^2 + \|\mu_{3,n}\|_2^2 \right) \\ &\quad - N(C_Y - C_E) \end{aligned} \quad (48)$$

Let us define the following functions

$$\tilde{\omega}_{\mathcal{C}}(\mu_0) = \arg \max_{\boldsymbol{\omega} : \gamma_{\mathcal{C}_i} \geq 0} \sum_{i=1}^K \left( \boldsymbol{\omega}_{\mathcal{C}_i}^\top \mathbf{B}_{\mathcal{C}}(\mu_0) \boldsymbol{\omega}_{\mathcal{C}_i} + \mathbf{c}_{\mathcal{C}_i}^\top \boldsymbol{\omega}_{\mathcal{C}_i} \right) \quad (49)$$

for the coarse scale problem, and

$$\tilde{\omega}(\mu_1, \mu_2) = \arg \max_{\boldsymbol{\omega} : \gamma_n \geq 0} \sum_{n=1}^N \left( \boldsymbol{\omega}_n^\top \mathbf{B}(\mu_1, \mu_2) \boldsymbol{\omega}_n + \mathbf{c}_n^\top \boldsymbol{\omega}_n \right) \quad (50)$$

for the fine scale problem. By substituting (49) in  $g_0$  and (50) in  $g_1$  and  $g_2$ , the optimal  $\mu_0, \mu_1$  and  $\mu_2$  can be found by solving two systems of equations, one for the coarse scale problem, given by:

$$\text{find } \mu_0 \text{ such that } g_0(\mu_0; \tilde{\omega}_{\mathcal{C}}) = 0 \quad (51)$$

and another for the fine scale problem, given by:

$$\text{find } \mu_1, \mu_2 \text{ such that } \begin{cases} g_1(\mu_1, \mu_2; \tilde{\omega}) = 0 \\ g_2(\mu_1, \mu_2; \tilde{\omega}) = 0 \end{cases} \quad (52)$$

where we omitted the dependency of functions  $\tilde{\omega}$  and  $\tilde{\omega}_{\mathcal{C}}$  on  $\mu_0, \mu_1$  and  $\mu_2$  for notational simplicity.

This consists basically of maximizing the inner optimization problem (with respect to  $\boldsymbol{\omega}$  or  $\boldsymbol{\omega}_{\mathcal{C}}$ ) such that the quadratic constraints of the primal problems are satisfied.

Although many techniques can be used to solve (51) (resp. (52)), care must be taken since evaluating functions  $\tilde{\omega}_{\mathcal{C}}(\mu_0)$  (resp.  $\tilde{\omega}(\mu_1, \mu_2)$ ) is computationally expensive. Thus, to have an efficient solution we resort to a bisection strategy, which is a robust algorithm that converges to approximate solutions to these problems with relatively few function evaluations.

Although the solution of (51) using the conventional bisection algorithm is straightforward, the multidimensional case is less clear. Thus, we present it in the remaining of this section.

The multidimensional bisection algorithm relies on the Poincaré-Miranda theorem, which states that if a set of multivariate functions change sign in an interval for any of its coordinates, then there is at least one root, common to all such functions, within that interval [50], [51]. This condition is then used to verify whether a given region in the function's domain contains a zero or not.

Thus, by defining a search space and dividing it in two along one of the coordinates, we can test to see in which half the root is contained. By performing this operation alternately along each of the function coordinates, we can get arbitrarily close to the root [50], [51]. This procedure is detailed in Algorithm 1. In all our experiments, we ran Algorithm 1 for ten iterations or until the relative variation of the parameters became smaller than a tolerance factor  $\epsilon = 0.1$ .

The final Blind Multiscale Unmixing Algorithm for Nonlinear spectral unmixing (BMUA-N) is presented in Algorithm 2.

$$B(\mu_1, \mu_2) = -\frac{1}{2} \begin{bmatrix} K + \frac{1}{\mu_1}I + \frac{1}{\mu_2}MM^\top & -K(M^\dagger)^\top & \frac{1}{\mu_2}M & -\frac{1}{\mu_2}M\mathbf{1} \\ -M^\dagger K & \frac{1}{\mu_2}I + M^\dagger K(M^\dagger)^\top & \mathbf{0} & \mathbf{0} \\ \frac{1}{\mu_2}M^\top & \mathbf{0} & \frac{1}{\mu_2}I & -\frac{1}{\mu_2}\mathbf{1} \\ -\frac{1}{\mu_2}\mathbf{1}^\top M^\top & \mathbf{0} & -\frac{1}{\mu_2}\mathbf{1}^\top & \frac{1}{\mu_2}P \end{bmatrix}, \quad \omega_n = \begin{bmatrix} \beta_n \\ \mu_{3,n} \\ \gamma_n \\ \lambda_n \end{bmatrix} \quad (44)$$

$$c_n = \left[ -a_{\mathcal{D}_n}^\top M^\top + y_n^\top \mid -\psi_{c_n}(M)^\top (M^\dagger)^\top \mid -a_{\mathcal{D}_n}^\top \mid \mathbf{1}^\top a_{\mathcal{D}_n} - 1 \right]$$

---

**Algorithm 1: Bi-dimensional bisection algorithm**


---

**Input :** Functions  $g_1, g_2 : \mathbb{R}^2 \rightarrow \mathbb{R}$ , .  
**Output:** The estimated root  $(a_r, b_r)$ .  
1 Define an initial rectangle containing the root  
 $R = \{(a_1, b_1), (a_2, b_1), (a_1, b_2), (a_2, b_2)\}$ ,  $a_1 < a_2$ ,  $b_1 < b_2$  ;  
2 **while** *Stopping criteria is not satisfied* **do**  
3   Compute centers:  $(a_c, b_c) = ((a_2 - a_1)/2, (b_2 - b_1)/2)$  ;  
4   Divide the search space in two and check for the root:  
 $R' = \{(a_1, b_1), (a_c, b_1), (a_1, b_2), (a_c, b_2)\}$  ;  
5   Evaluate  $g_1$  and  $g_2$  at the four vertices of  $R'$  ;  
6   **if** *the sign of both  $g_1$  and  $g_2$  is not constant at all vertices of  $R'$*  **then**  
7      $a_2 = a_c$  ;  
8   **else**  
9      $a_1 = a_c$   
10   **end**  
11   Partition rectangle across the other dimension  
 $R' = \{(a_1, b_1), (a_2, b_1), (a_1, b_c), (a_2, b_c)\}$  ;  
12   Evaluate  $g_1$  and  $g_2$  at the four vertices of  $R'$  ;  
13   **if** *the sign of both  $g_1$  and  $g_2$  is not constant at all vertices of  $R'$*  **then**  
14      $b_2 = b_c$  ;  
15   **else**  
16      $b_1 = b_c$   
17   **end**  
18 **end**  
19  $(a_r, b_r) = ((a_2 - a_1)/2, (a_2 - a_1)/2)$  ;  
20 **return**  $(a_r, b_r)$ ;

---



---

**Algorithm 2: BMUA-N**


---

**Input :**  $Y$ ,  $M$ ,  $\sigma_{e,\psi}^2$ , the number of superpixels  $K$  and multiscale decomposition matrix  $W$ .  
**Output:** The estimated abundance matrix  $\hat{A}$ .  
1 Estimate the noise covariance matrix  $\Sigma_e$  from  $Y$  ;  
2 Compute the constants  $C_0$ ,  $C_1$ ,  $C_Y$  and  $C_E$  using equations (22), (20), and (33) ;  
3 Compute  $Y_C = YW$  ;  
4 Find  $\hat{A}_C$  by solving (10) using the procedures detailed in Sections (V-A) and (V-C);  
5 Compute  $\hat{A}_D$  using (11);  
6 Find  $\hat{A}$  by solving (35) using the procedures detailed in sections (V-B) and (V-C);  
7 **return**  $\hat{A}$ ;

---

## VI. DETERMINING THE NUMBER OF SUPERPIXELS

A parameter of fundamental importance in the design of the proposed multiscale transform  $W$  is the number of superpixels  $K$ , or, equivalently, the average size of each superpixel  $S = N/K$ . The purpose of the multiscale transform is to group semantically/spectrally similar pixels, which are then

averaged (within each superpixel) to constitute the coarse scale image, capturing spatial correlation and reducing the influence of noise. From this definition, the desired average superpixel size could be intuitively defined as the largest value of  $S$  such that the superpixels are still spectrally homogeneous.

In order to evaluate the homogeneity of the superpixels, we consider the distribution of the singular values of the sets of pixels within each superpixel, which are ordered in the form of matrices (matricized). Thus, the  $j$ -th matricized superpixel  $Y_j$  can be written as

$$Y_j = [y_{I_1}, \dots, y_{I_{|\mathcal{N}_j|}}], \quad \{I_1, \dots, I_{|\mathcal{N}_j|}\} \subseteq \mathcal{N}_j \quad (53)$$

for  $j = 1, \dots, K$ . Denote the singular values of  $Y_j$  by  $\rho_{j,1}, \rho_{j,2}, \dots, \rho_{j,|\mathcal{N}_j|}$ , ordered from the largest to the smallest magnitude.

In order to evaluate the superpixel homogeneity, we measure how close the matrices  $Y_j$  are to being of rank-1 by computing the ratio between the two largest singular values as [52]:

$$Hom(K) = \frac{1}{K} \sum_{j=1}^K \frac{|\rho_{j,1}|}{|\rho_{j,2}|} \quad (54)$$

where  $Hom(K)$  is the average homogeneity of all superpixels as a function of the number of superpixels  $K$  and we assume that  $\rho_{j,2}$  exists and is nonzero. The ratio between the largest singular values has already been successfully employed to detect heterogeneous superpixels in HS segmentation [52].

Thus, the number of superpixels can be selected using the following simple criterion:

$$K = \max_j \quad \text{subject to } Hom(j) \geq (1 - \varepsilon) \max_v \{Hom(v)\} \quad (55)$$

$$K_{\min} \leq j \leq K_{\max}$$

where we restrict the number of superpixels to be within a prescribed interval  $[K_{\min}, K_{\max}]$ .

## VII. RESULTS

In this section, we evaluate the performance of the proposed method using both synthetic and real datasets. The BMUA-N is compared with the fully constrained least squares (FCLS), with the unregularized K-Hype [20] and with the Total Variation-based K-Hype algorithms (K-Hype-TV) [31]. The performances were evaluated using the Root Means Squared Error (RMSE) between the estimated abundance maps ( $RMSE_A$ ) and between the reconstructed images ( $RMSE_Y$ ).

The RMSE between a true, generic matrix  $\mathbf{X}$  and its estimate  $\hat{\mathbf{X}}$  is defined as

$$\text{RMSE}_{\mathbf{X}} = \sqrt{\frac{1}{N_{\mathbf{X}}} \|\mathbf{X} - \hat{\mathbf{X}}\|_F^2} \quad (56)$$

where  $N_{\mathbf{X}}$  denotes the number of elements in the matrix  $\mathbf{X}$ .

For the proposed method, the noise covariance matrix  $\Sigma_e$  was estimated using the residual method described in [53], [54], and the superpixel sizes were selected using the strategy detailed in Section VI, with  $K_{\min} = N/8$ ,  $K_{\max} = N/170$  and  $\varepsilon = 0.1$ . The polynomial kernel described in (6) was used with  $d = 2$  for all non-linear SU algorithms.

Table I  
QUANTITATIVE RESULTS FOR DATA CUBES DC1 AND DC2.

DC1 data cube					
SNR	Method	BLMM		PNMM	
		RMSE <sub>A</sub>	RMSE <sub>Y</sub>	RMSE <sub>A</sub>	RMSE <sub>Y</sub>
20dB	FCLS	0.2587	1.7102	0.1657	1.5529
	K-Hype	0.0575	1.2207	0.0972	1.1506
	K-Hype-TV	0.0371	<b>1.2180</b>	0.0800	<b>1.1466</b>
	BMUA-N	<b>0.0326</b>	1.2273	<b>0.0730</b>	1.1588
30dB	FCLS	0.2591	1.2516	0.1633	1.0944
	K-Hype	0.0346	0.3863	0.0765	<b>0.3629</b>
	K-Hype-TV	<b>0.0323</b>	0.3864	0.0763	<b>0.3629</b>
	BMUA-N	0.0325	<b>0.3841</b>	<b>0.0734</b>	0.3638

DC2 data cube					
SNR	Method	BLMM		PNMM	
		RMSE <sub>A</sub>	RMSE <sub>Y</sub>	RMSE <sub>A</sub>	RMSE <sub>Y</sub>
20dB	FCLS	0.1718	1.5783	0.1554	1.5461
	K-Hype	0.0723	1.1591	0.1165	<b>1.1343</b>
	K-Hype-TV	0.0557	<b>1.1541</b>	0.1037	<b>1.1343</b>
	BMUA-N	<b>0.0491</b>	1.1544	<b>0.1009</b>	1.1363
30dB	FCLS	0.1714	1.1218	0.1553	1.0941
	K-Hype	0.0504	0.3653	0.0994	<b>0.3592</b>
	K-Hype-TV	0.0501	0.3653	0.0992	<b>0.3592</b>
	BMUA-N	<b>0.0393</b>	0.3654	<b>0.0902</b>	0.3604

#### A. Synthetic data sets

To compare the performance of the different algorithms quantitatively, we created two synthetic datasets with spatially correlated abundance maps, namely Data Cube 0 (DC0), with  $70 \times 70$  pixels, and Data Cube 1 (DC1), with  $50 \times 50$  pixels. Both datasets were constructed using three spectral signatures with 224 bands extracted from the USGS Spectral Library. The synthetic abundance maps are displayed in the first row of Figs. 2 and 3.

The reflectance values were generated using two nonlinear mixture models, namely, the bilinear mixing model (BLMM), defined as

$$\mathbf{y}_n = \mathbf{M}\mathbf{a}_n + \sum_{i=1}^{P-1} \sum_{j=i+1}^P a_{n,i}a_{n,j}\mathbf{m}_i \circ \mathbf{m}_j + \mathbf{e}_n \quad (57)$$

with  $\circ$  being the Hadamard product, and the post-nonlinear mixing model (PNMM), defined as

$$\mathbf{y}_n = (\mathbf{M}\mathbf{a}_n)^{0.7} + \mathbf{e}_n \quad (58)$$

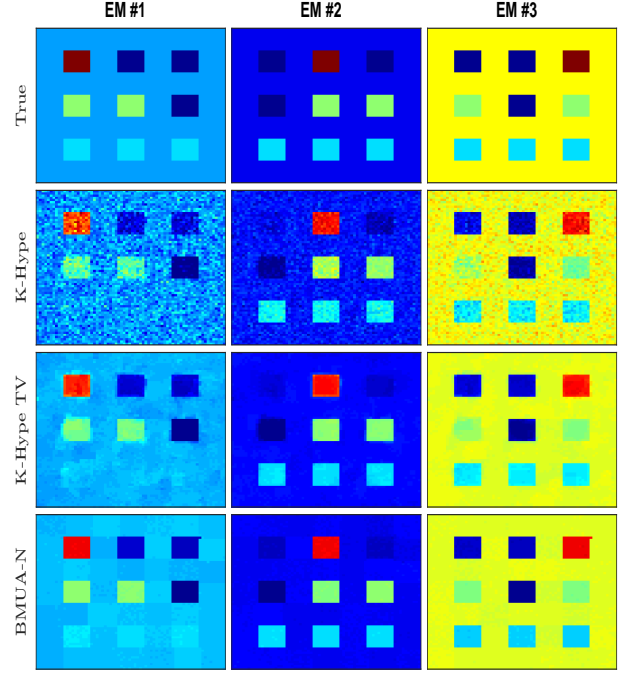


Figure 2. Abundance maps estimated by all algorithms for the DC1 data cube, with abundance values scaled between  $\alpha_k = 0$  (blue) and  $\alpha_k = 1$  (red).

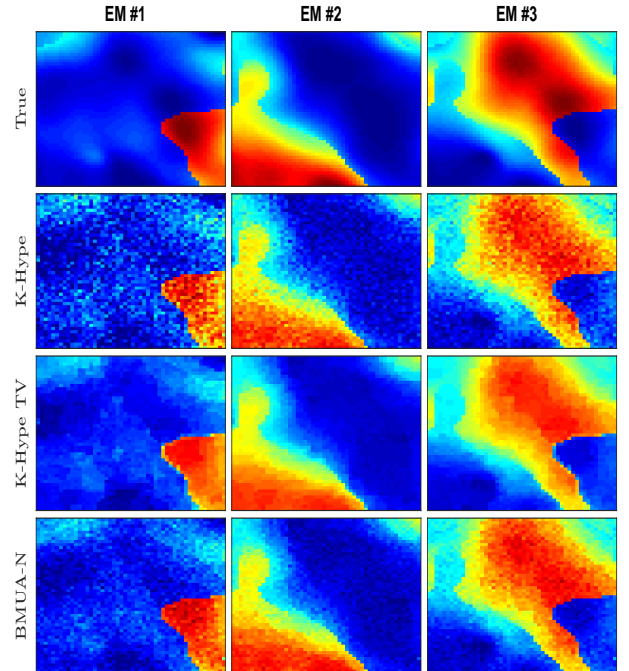


Figure 3. Abundance maps estimated by all algorithms for the DC2 data cube, with abundance values scaled between  $\alpha_k = 0$  (blue) and  $\alpha_k = 1$  (red).

where a fixed exponential value of 0.7 has been applied to the LMM result. Finally, white Gaussian noise with signal to noise ratios (SNR) of both 20 and 30dB was added to all datasets.

The parameters for each algorithm were either fixed or selected based on a grid search performed for each dataset, with search ranges defined based on those ranges discussed by the authors in the original publications. For the BMUA-N, we fixed the modeling errors as a small value relative to the average pixel energy, given by  $\sigma_{e,\psi}^2 = 10^{-8} \frac{1}{N} \sum_{n=1}^N \|\mathbf{y}_n\|_2^2$ . For the K-Hype algorithm, we selected the parameter among the values  $\mu \in \{0.001, 0.002, 0.005, 0.01, 0.02, 0.1, 1\}$ . For the K-Hype-TV, the parameters were selected among the following values:  $\mu \in \{0.001, 0.002, 0.005, 0.01, 0.02, 0.1, 1\}$ ,  $\eta \in \{0, 0.01, 0.1, 0.25, 0.5, 0.75, 1\}$ .

1) *Discussion:* The quantitative results of all algorithms are shown in Table I. The proposed BMUA-N method outperformed the competing algorithms for almost all cases, except for one where its result was very close to those of the TV-based solution. This is despite the fact that the parameters of K-Hype and K-Hype-TV were selected through a grid search procedure.

The abundance maps provided by the nonlinear SU methods for both datacubes are displayed in Figures 2 and 3 for illustrative purposes for the case of the BLMM with an SNR of 20dB. The FCLS results were not displayed for the sake of space since they were significantly worse than those of the other algorithms. It can be seen that the BMUA-N results better approximates the ground truth, and even though the K-Hype-TV solution is smoother for DC2 its mean results are farther from the true values. The reconstruction errors of the nonlinear SU algorithms, also shown in Table I, were similar and significantly lower than those of the FCLS. The execution times of the BMUA-N algorithm, shown in Table II, are about 3.5 times higher than those of K-Hype-TV. Thus, the complexity of the BMUA-N is still on the same order of the TV-based solution even though no significant parameter tuning is necessary.

Table II  
AVERAGE EXECUTION TIME (IN SECONDS) OF THE UNMIXING ALGORITHMS.

	DC1	DC2	Cuprite
FCLS	0.694	0.326	16.302
K-Hype	4.836	2.271	41.087
K-Hype-TV	45.805	23.33	425.964
BMUA-N	161.321	86.413	1507.039

Table III  
RECONSTRUCTION ERRORS (RMSE<sub>Y</sub>) FOR THE CUPRITE DATA SET.

	FCLS	K-Hype	K-Hype-TV	BMUA-N
Cuprite	0.1466	<b>0.1123</b>	0.1127	0.1227

### B. Experiments with real data

For the simulations with real data we consider the Cuprite dataset, which was captured by the AVIRIS instrument and originally had 224 bands. Water absorption and low SNR

bands were removed before processing, resulting in 188 bands. Previous works indicate that 14 endmembers are present at the Cuprite mining field [55], [28], [34]. We used the same endmember signatures as in [28], [34]. The reconstructed abundance maps of the nonlinear SU algorithms are presented in Figure 4, where four endmembers whose distribution could be clearly distinguished in the scene were selected [55]. The results for all depicted algorithms are generally compatible and agree with previous studies of this scene [55], [28], [34]. Nevertheless, a careful analysis reveal that the BMUA-N results, displayed in the bottom row of Figure 4, show smoother abundance reconstructions without compromising image details and discontinuities.

The reconstruction errors for the Cuprite dataset are shown in Table III, with considerably smaller errors for the nonlinear SU algorithms when compared to the FCLS. The execution times of the proposed method were again around 3.5 times higher than that of the TV-based solution, which indicates that it scales favorably with larger image sizes.

## VIII. CONCLUSIONS

In this paper, a blind multiscale unmixing strategy was proposed for nonlinear kernel-based mixing models. Based on the concept of a multiscale regularization strategy recently introduced in [33], we were able to efficiently capture image spatial information by splitting the nonlinear mixing process between two image scales, one containing the coarse, low-dimensional image structures and another representing the original image domain. Furthermore, we employed a theory-based statistical framework to devise a consistent strategy to automatically select the regularization parameters of the proposed algorithm and of the multiscale transformation. This resulted in a truly blind (from the parameter setting perspective) multiscale regularization framework. The unmixing problem was formulated using quadratically constrained optimization problems, for which efficient solutions were obtained by exploring a reformulation of their dual representations as root-finding problems. Simulation results with both synthetic and real data indicate that the proposed strategy leads to a consistent performance improvement when compared to the classical Total Variation regularization, even though no parameter adjustment is necessary.

## REFERENCES

- [1] J. M. Bioucas-Dias, A. Plaza, G. Camps-Valls, P. Scheunders, N. Nasrabadi, and J. Chanussot, "Hyperspectral remote sensing data analysis and future challenges," *IEEE Geoscience and Remote Sensing Magazine*, vol. 1, no. 2, pp. 6–36, 2013.
- [2] N. Dobigeon, J.-Y. Tourneret, C. Richard, J. C. M. Bermudez, S. McLaughlin, and A. O. Hero, "Nonlinear unmixing of hyperspectral images: Models and algorithms," *IEEE Signal Processing Magazine*, vol. 31, no. 1, pp. 82–94, Jan 2014.
- [3] T. Imbiriba, J. C. M. Bermudez, C. Richard, and J.-Y. Tourneret, "Nonparametric detection of nonlinearly mixed pixels and endmember estimation in hyperspectral images," *IEEE Transactions on Image Processing*, vol. 25, no. 3, pp. 1136–1151, March 2016.
- [4] B. Somers, G. P. Asner, L. Tits, and P. Coppin, "Endmember variability in spectral mixture analysis: A review," *Remote Sensing of Environment*, vol. 115, no. 7, pp. 1603–1616, 2011.

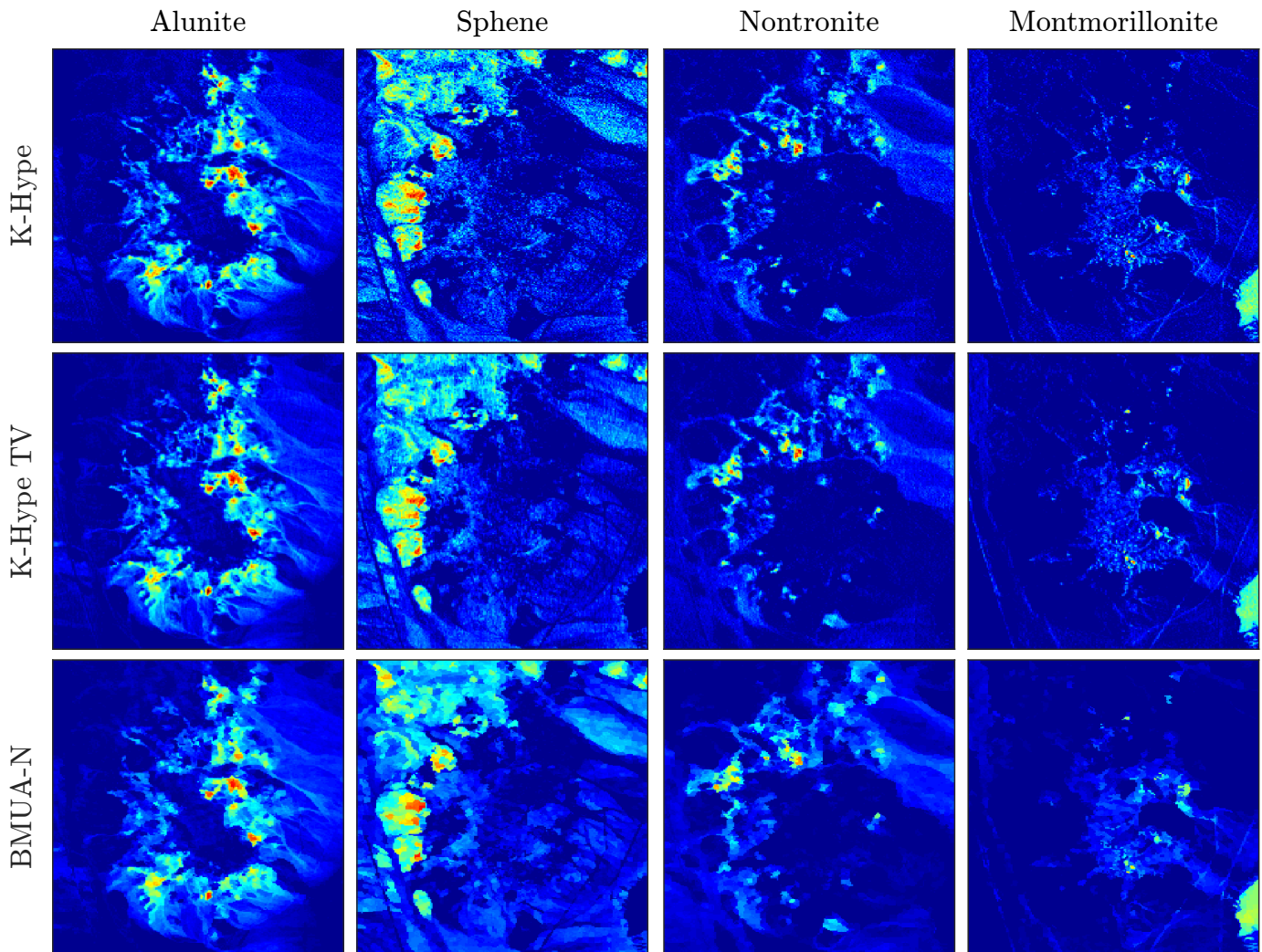


Figure 4. Abundance maps estimated by all algorithms for four endmembers of the Cuprite image, with abundance values scaled between  $\alpha_k = 0$  (blue) and  $\alpha_k = 1$  (red).

- [5] T. Imbiriba, R. A. Borsoi, and J. C. M. Bermudez, "Generalized linear mixing model accounting for endmember variability," in *2018 IEEE International Conference on Acoustics, Speech and Signal Processing (ICASSP)*. IEEE, 2018, pp. 1862–1866.
- [6] R. A. Borsoi, T. Imbiriba, and J. C. Moreira Bermudez, "Super-Resolution for Hyperspectral and Multispectral Image Fusion Accounting for Seasonal Spectral Variability," *ArXiv e-prints*, Aug. 2018.
- [7] R. A. Borsoi, T. Imbiriba, and J. C. M. Bermudez, "Deep generative end-member modeling: An application to unsupervised spectral unmixing," *arXiv preprint arXiv:1902.05528*, 2019.
- [8] P.-A. Thouvenin, N. Dobigeon, and J.-Y. Tourneret, "Hyperspectral unmixing with spectral variability using a perturbed linear mixing model," *IEEE Transactions on Signal Processing*, vol. 64, no. 2, pp. 525–538, Feb. 2016.
- [9] T. W. Ray and B. C. Murray, "Nonlinear spectral mixing in desert vegetation," *Remote Sensing of Environment*, vol. 55, no. 1, pp. 59–64, 1996.
- [10] R. Heylen, M. Parente, and P. Gader, "A review of nonlinear hyperspectral unmixing methods," *IEEE Journal of Selected Topics in Applied Earth Observations and Remote Sensing*, vol. 7, no. 6, pp. 1844–1868, June 2014.
- [11] J. F. Mustard and C. M. Pieters, "Photometric phase functions of common geologic minerals and applications to quantitative analysis of mineral mixture reflectance spectra," *Journal of Geophysical Research: Solid Earth*, vol. 94, no. B10, pp. 13 619–13 634, 1989.
- [12] K. J. Guilfoyle, M. L. Althouse, and C.-I. Chang, "A quantitative and comparative analysis of linear and nonlinear spectral mixture models using radial basis function neural networks," *IEEE Transactions on Geoscience and Remote Sensing*, vol. 39, no. 10, pp. 2314–2318, 2001.
- [13] Y. Altmann, A. Halimi, N. Dobigeon, and J. Y. Tourneret, "Supervised nonlinear spectral unmixing using a postnonlinear mixing model for hyperspectral imagery," *IEEE Transactions on Image Processing*, vol. 21, no. 6, pp. 3017–3025, June 2012.
- [14] P.-X. Li, B. Wu, and L. Zhang, "Abundance estimation from hyperspectral image based on probabilistic outputs of multi-class support vector machines," in *2005 IEEE International Geoscience and Remote Sensing Symposium (IGARSS)*, vol. 6, July 2005, pp. 4315–4318.
- [15] R. Heylen, D. Burazerovic, and P. Scheunders, "Non-linear spectral unmixing by geodesic simplex volume maximization," *IEEE Journal of Selected Topics in Signal Processing*, vol. 5, no. 3, pp. 534–542, 2011.
- [16] R. Heylen and P. Scheunders, "A distance geometric framework for nonlinear hyperspectral unmixing," *IEEE Journal of Selected Topics in Applied Earth Observations and Remote Sensing*, vol. 7, no. 6, pp. 1879–1888, June 2014.
- [17] X. Wu, X. Li, and L. Zhao, "A kernel spatial complexity-based nonlinear unmixing method of hyperspectral imagery," in *Proc. LSMS/ICSEE*, 2010, pp. 451–458. [Online]. Available: <http://portal.acm.org/citation.cfm?id=1888593.1888651>
- [18] X. Li, J. Cui, and L. Zhao, "Blind nonlinear hyperspectral unmixing based on constrained kernel nonnegative matrix factorization," *Signal, Image and Video Processing*, vol. 8, no. 8, pp. 1555–1567, 2012.
- [19] J. Chen, C. Richard, and P. Honeine, "Nonlinear unmixing of hyperspectral data based on a linear-mixture/nonlinear-fluctuation model," *IEEE Transactions on Signal Processing*, vol. 61, pp. 480–492, Jan 2013.

- [20] —, “Nonlinear estimation of material abundances in hyperspectral images with  $\ell_1$ -norm spatial regularization,” *IEEE Transactions on Geoscience and Remote Sensing*, vol. 52, no. 5, pp. 2654–2665, May 2014.
- [21] Y. Altmann, N. Dobigeon, S. McLaughlin, and J.-Y. Tourneret, “Nonlinear spectral unmixing of hyperspectral images using gaussian processes,” *IEEE Transactions on Signal Processing*, vol. 61, pp. 2442–2453, May 2013.
- [22] R. Ammanouil, A. Ferrari, C. Richard, and S. Mathieu, “Nonlinear unmixing of hyperspectral data with vector-valued kernel functions,” *IEEE Transactions on Image Processing*, vol. 26, no. 1, pp. 340–354, 2017.
- [23] C. Shi and L. Wang, “Incorporating spatial information in spectral unmixing: A review,” *Remote Sensing of Environment*, vol. 149, pp. 70–87, 2014.
- [24] T. Imbiriba, R. A. Borsoi, and J. C. M. Bermudez, “A low-rank tensor regularization strategy for hyperspectral unmixing,” in *2018 IEEE Statistical Signal Processing Workshop (SSP)*, 2018, pp. 373–377.
- [25] M.-D. Iordache, J. M. Bioucas-Dias, and A. Plaza, “Total variation spatial regularization for sparse hyperspectral unmixing,” *IEEE Transactions on Geoscience and Remote Sensing*, vol. 50, no. 11, pp. 4484–4502, 2012.
- [26] R. Feng, Y. Zhong, and L. Zhang, “Adaptive spatial regularization sparse unmixing strategy based on joint map for hyperspectral remote sensing imagery,” *IEEE Journal of Selected Topics in Applied Earth Observations and Remote Sensing*, vol. 9, no. 12, pp. 5791–5805, 2016.
- [27] L. Drumetz, M.-A. Veganzones, S. Henrot, R. Phlypo, J. Chanussot, and C. Jutten, “Blind hyperspectral unmixing using an extended linear mixing model to address spectral variability,” *IEEE Transactions on Image Processing*, vol. 25, no. 8, pp. 3890–3905, 2016.
- [28] T. Imbiriba, R. A. Borsoi, and J. C. M. Bermudez, “Low-rank tensor modeling for hyperspectral unmixing accounting for spectral variability,” *arXiv preprint arXiv:1811.02413*, 2018.
- [29] R. A. Borsoi, T. Imbiriba, and J. C. Moreira Bermudez, “Improved hyperspectral unmixing with endmember variability parametrized using an interpolated scaling tensor,” in *2019 IEEE International Conference on Acoustics, Speech and Signal Processing (ICASSP)*, May 2019, pp. 2177–2181.
- [30] M. Tang, L. Gao, A. Marinoni, P. Gamba, and B. Zhang, “Integrating spatial information in the normalized p-linear algorithm for nonlinear hyperspectral unmixing,” *IEEE Journal of Selected Topics in Applied Earth Observations and Remote Sensing*, vol. 11, no. 4, pp. 1179–1190, 2018.
- [31] J. Chen, C. Richard, and P. Honeine, “Nonlinear estimation of material abundances in hyperspectral images with  $L_1$ -norm spatial regularization,” *Geoscience and Remote Sensing, IEEE Transactions on*, vol. 52, no. 5, pp. 2654–2665, 2014.
- [32] R. Wang, H.-C. Li, W. Liao, X. Huang, and W. Philips, “Centralized collaborative sparse unmixing for hyperspectral images,” *IEEE Journal of Selected Topics in Applied Earth Observations and Remote Sensing*, vol. 10, no. 5, pp. 1949–1962, 2017.
- [33] R. A. Borsoi, T. Imbiriba, J. C. M. Bermudez, and C. Richard, “A fast multiscale spatial regularization for sparse hyperspectral unmixing,” *IEEE Geoscience and Remote Sensing Letters*, vol. 16, no. 4, pp. 598–602, April 2019.
- [34] R. A. Borsoi, T. Imbiriba, and J. C. Moreira Bermudez, “A Data Dependent Multiscale Model for Hyperspectral Unmixing With Spectral Variability,” *ArXiv e-prints*, Aug. 2018.
- [35] Y. Song, D. Brie, E.-H. Djermoune, and S. Henrot, “Regularization parameter estimation for non-negative hyperspectral image deconvolution,” *IEEE Transactions on Image Processing*, vol. 25, no. 11, pp. 5316–5330, 2016.
- [36] J. Mercer, “Functions of positive and negative type and their connection with the theory of integral equations,” *Philos. Trans. Roy. Soc. London Ser. A*, vol. 209, pp. 415–446, 1909.
- [37] E. H. Moore, “On properly positive hermitian matrices,” *Bull. American Mathematical Society*, vol. 23, p. 59, 1916.
- [38] N. Aronszajn, “Theory of reproducing kernels,” *Transactions of the American Mathematical Society*, vol. 68, 1950.
- [39] E. Kreyszig, *Introductory functional analysis with applications*. Wiley New York, 1989, vol. 81.
- [40] I. Steinwart and A. Christmann, *Support vector machines*. Springer, 2008.
- [41] V. N. Vapnik, *The nature of statistical learning theory*. New York, NY: Springer, 1995.
- [42] B. Schölkopf and A. J. Smola, *Learning with Kernels: Support Vector Machines, Regularization, Optimization, and Beyond*. The MIT Press, 2001.
- [43] C. E. Rasmussen and C. K. I. Williams, *Gaussian Processes for Machine Learning*. The MIT Press, 2006.
- [44] B. Somers, K. Cools, S. Delalieux, J. Stuckens, D. V. der Zande, W. W. Verstraeten, and P. Coppin, “Nonlinear hyperspectral mixture analysis for tree cover estimates in orchards,” *Remote Sensing of Environment*, vol. 113, no. 6, pp. 1183–1193, February 2009.
- [45] J. A. K. Suykens, T. V. Gestel, J. D. Brabanter, B. D. Moor, and J. Vandewalle, *Least Squares Support Vector Machines*. Singapore: World Scientific, 2002.
- [46] R. Achanta, A. Shaji, K. Smith, A. Lucchi, P. Fua, and S. Süsstrunk, “SLIC superpixels compared to state-of-the-art superpixel methods,” *IEEE Transactions on Pattern Analysis and Machine Intelligence*, vol. 34, no. 11, pp. 2274–2282, 2012.
- [47] Y. Altmann, M. Pereyra, and S. McLaughlin, “Bayesian nonlinear hyperspectral unmixing with spatial residual component analysis,” *IEEE Transactions on Computational Imaging*, vol. 1, no. 3, pp. 174–185, 2015.
- [48] R. Ammanouil, A. Ferrari, C. Richard, and J.-Y. Tourneret, “Spatial regularization for nonlinear unmixing of hyperspectral data with vector-valued kernel functions,” in *2016 IEEE Statistical Signal Processing Workshop (SSP)*. IEEE, 2016, pp. 1–5.
- [49] S. Boyd and L. Vandenberghe, *Convex optimization*. Cambridge university press, 2004.
- [50] M. L. Galván, “The multivariate bisection algorithm,” *arXiv preprint arXiv:1702.05542*, 2017.
- [51] D. Bachrathy and G. Stépán, “Bisection method in higher dimensions and the efficiency number,” *Periodica Polytechnica Mechanical Engineering*, vol. 56, no. 2, pp. 81–86, 2012.
- [52] J. Yi and M. Velez-Reyes, “Low-dimensional enhanced superpixel representation with homogeneity testing for unmixing of hyperspectral imagery,” in *Algorithms and Technologies for Multispectral, Hyperspectral, and Ultraspectral Imagery XXIV*, vol. 10644. International Society for Optics and Photonics, 2018, p. 1064422.
- [53] R. E. Roger, “Principal components transform with simple, automatic noise adjustment,” *International Journal of Remote Sensing*, vol. 17, no. 14, pp. 2719–2727, 1996.
- [54] A. Mahmood, A. Robin, and M. Sears, “Modified residual method for the estimation of noise in hyperspectral images,” *IEEE Transactions on Geoscience and Remote Sensing*, vol. 55, no. 3, pp. 1451–1460, 2017.
- [55] J. M. P. Nascimento and J. M. Bioucas-Dias, “Vertex Component Analysis: A fast algorithm to unmix hyperspectral data,” *IEEE Transactions on Geoscience and Remote Sensing*, vol. 43, no. 4, pp. 898–910, April 2005.